TOPEX/Poseidon Microwave Radiometer (TMR): II. Antenna Pattern Correction and Brightness Temperature Algorithm

Michael A. Janssen, Christopher S. Ruf, *Senior Member, IEEE,* and Stephen J. Keihm

***Abstract*— The calibrated antenna temperatures measured by the TOPEX Microwave Radiometer are used to derive radiometric brightness temperatures in the vicinity of the altimeter footprint. The basis for the procedure devised to do this—the antenna pattern correction and brightness temperature algorithm—is described in this paper, along with its associated uncertainties. The algorithm is based on knowledge of the antenna pattern, the ground-based measurements of which are presented along with their analyses. Using the results of these measurements, we perform an error analysis that yields the net uncertainties in the derived TMR footprint brightness temperatures. The net brightness temperature uncertainties range from 0.79 to 0.88°K for the three TMR frequencies, and include the radiometer calibration uncertainties which range from 0.54 to 0.57°K. We also derive an estimate of the uncertainty incurred by using brightness temperatures measured in the ~40 km TMR footprint to estimate path delay in the ~3 km altimeter footprint. The RMS difference in path delay averaged over the largest TMR footprint relative to that in the altimeter footprint is estimated to be about 0.3 cm. Finally, we discuss the error associated with using unequal beams at the three TMR frequencies to derive path delays, and describe an approach using along-track averaging of the algorithm brightness temperatures to reduce this error.**

I. Introduction

THE correction to account for the variable path delay due to atmospheric water vapor depends on the accurate measurement of brightness temperature at the TMR frequencies in the vicinity of the altimeter footprint. This paper describes how brightness temperatures are estimated from calibrated antenna temperatures, and gives the associated uncertainties. The TOPEX Microwave Radiometer and its calibration to provide accurate antenna temperatures are described in [1]. The brightness temperatures are in turn used to provide path delay corrections as discussed in [2].

The three-channel TMR and its antenna is a reduced version of the ten-channel Scanning Multichannel Microwave Radiometer (SMMR) flown on Seasat and Nimbus-7 [3]. The TMR was built almost entirely from spare SMMR flight parts. The SMMR was designed to provide full mapping of both ocean and atmospheric parameters, while the objective of the TMR is specifically to provide the nadir propagation path delay due to atmospheric water vapor. Single polarizations at the SMMR frequencies 18, 21, and 37 GHz are sufficient for this task, so that only the components to provide single channels at these frequencies were used (along with a redundant backup channel at 21 GHz). The SMMR scanning mechanism was replaced by a fixed antenna, although the same offset paraboloid antenna and support structure were used.

The TMR was further modified to improve its performance based on SMMR flight experience [4]–[6]. Early analyses of existing SMMR antenna patterns [4] indicated that the sidelobe power levels would lead to significant contributions off the beam axis that could not be adequately modeled in the antenna pattern correction. Because these sidelobes were largely the result of interference from the antenna support legs at the edge of the signal path, the TMR feed was redesigned to slightly underilluminate the aperture relative to SMMR to reduce this interference. The redesign was relatively straightforward because the TMR feed needed to accommodate fewer frequencies spanning a reduced range. Other modifications included a sun screen and a radom over the feed to reduce thermal excursions and consequent radiometric instabilities due to periodic solar heating [5], [6]. Further details of these modifications and a comparison between the SMMR and TMR antenna performances are given in [1].

II. Antenna Pattern Correction Algorithm

The antenna temperature T_a is proportional to the power collected by the antenna and input to the receiver [7]. In particular, it may be described as an integration of the product of radiant intensity, or brightness temperature, with the antenna gain, summed over all directions, or

$$T_a(\Omega) = \int_{4\pi} T_b(\Omega') G(\Omega', \Omega) d\Omega' \tag{1}$$

where $T_b(\Omega')$ is the brightness temperature in the direction of the element of solid angle $d\Omega'$, and $G(\Omega', \Omega)$ is the gain of the antenna in the direction Ω' for an antenna pointed in the direction Ω. The gain pattern is normalized so that

$$\int_{4\pi} G(\Omega', \Omega)\, d\Omega' = 1. \tag{2}$$

Manuscript received September 7, 1993; revised April 12, 1994. This work presents the results of one phase of research conducted at the Jet Propulsion Laboratory, California Institute of Technology, Pasadena, CA, under contract to the National Aeronautics and Space Administration.

M. A. Janssen is with the Jet Propulsion Laboratory, California Institute of Technology, Pasadena, CA 91109 USA.

C. S. Ruf is with the Department of Electrical Engineering, The Pennsylvania State University, University Park, PA 16802 USA.

S. J. Kiehm is with Ball Corporation under contract to the Jet Propulsion Laboratory, California Institute of Technology, Pasadena, CA 91109 USA.

IEEE Log Number 9406437.

Ideally, the antenna temperature T_a is measured in all directions and the antenna gain pattern G is known, and the brightness temperature distribution T_b is obtained by inversion of (1). This can only be done approximately for the TMR data. First, measurement noise practically limits the angular resolution of the derived $T_b(\Omega')$ to about the width of the convolving function $G(\Omega', \Omega)$, which in our case is the half-power beamwidth of the TMR antenna. Expressed in terms of kilometers on the ground seen at nadir from the TOPEX orbit, this width is 43.4 km at 18 GHz, 36.4 km at 21 GHz, and 22.9 km at 37 GHz, whereas the effective altimeter footprint diameter is on the order of 3 km [8]. Secondly, the TMR only measures the antenna temperature along the nadir track of the TOPEX satellite, and the Seasat SMMR matrix inversion approach [6] that is made possible by its cross-track scanning capability is not applicable here. Finally, errors in our knowledge of the antenna gain pattern will lead to further errors in the inversion.

We have developed an approximate inversion that takes advantage of the facts that 1) most of the power in the TMR beams is concentrated within one or two beamwidths of the pointing direction, whereas the remaining power is distributed more or less uniformly across the Earth and cold sky, and 2) the combination of circular orbit and nadir viewing provides a stable geometry with time. The half-power beamwidths are 1.86°, 1.56°, and 0.98° at 18, 21, and 37 GHz, respectively [1]. Assuming that the brightness temperature is relatively uniform within a few beamwidths of the beam center, we may approximate (1) as

$$T_a = (1 - b - c)T_{\mathrm{mb}} + bT_e + cT_c \tag{3}$$

where

T_{mb} = mean brightness temperature within the main beam,
T_e = mean brightness temperature outside the main beam but within the Earth's limb,
T_c = mean brightness temperature beyond the Earth's limb

and the quantities b and c represent the beam fractions outside the main beam but within the Earth's limb, and beyond the Earth's limb respectively. Specifically,

$$b = 2\pi \int_0^{2\pi} \int_{\theta_1}^{\theta_2} G(\theta, \phi) \sin(\theta) d\theta \, d\phi \tag{4}$$

$$c = 2\pi \int_0^{2\pi} \int_{\theta_2}^{\pi} G(\theta, \phi) \sin(\theta) d\theta \, d\phi \tag{5}$$

where θ and ϕ are spherical coordinates with polar angle $\theta = 0$ along the beam axis. The polar angle limit θ_2 is about 55° as determined by the altitude of the TOPEX satellite. The main beam limit θ_1 is somewhat arbitrary because the performance of the algorithm is insensitive to its exact choice. We find that $\theta_1 = 10°$ easily includes the dominant portion of the main beam near the altimeter footprint, and ensures that the major contribution from the bT_e term is from distant regions of the Earth that are largely uncorrelated with the scene of interest.

Equation (3) may be readily inverted to obtain

$$T_{\mathrm{mb}} = \frac{1}{1 - b - c}(T_a - bT_e - cT_c). \tag{6}$$

Our approximation is to 1) determine the beam fractions b and c from range measurements of the flight antenna beam pattern, 2) estimate T_a and T_e from radiative transfer models and take T_c to be the cosmic microwave background brightness temperature, and 3) use T_{mb} as the best estimate of the mean brightness temperature within the altimeter footprint. Uncertainties associated with this procedure are discussed in following sections.

III. Antenna Pattern Measurement

A. Range Measurements

The antenna pattern at each of the three TMR frequencies was measured at JPL's antenna test range for the flight antenna/feed combination as well as for the flight spare antenna/feed combination. The range used was one of several at this facility, and features an East/West transmission path across a ravine cut into a hillside also running East/West. The range was therefore open to the South and well depressed beneath the transmission path, but contained some potential scattering paths from trees on the hillside to the North. The separation D of the transmitter from the antenna was 366 m, sufficiently exceeding the far-field distance to ignore near-field corrections (the far-field distance is $2\,d^2/\lambda = 154$ m at 37 GHz, where d is the 79-cm TMR antenna diameter).

The antenna/feed combination along with the feed cover and sunshield were mounted on a positioner capable of 360° movement in both azimuth and rotation. The beam patterns were measured using the positioner to scan the antenna horizontally across the transmitter from −180° to +180° in azimuth for selected rotations of the antenna about the RF boresight. The transmitter polarization was rotated for each scan to be either aligned with or orthogonal to the receiver polarization, so that both the co- and cross-polarized patterns were measured. The antenna RF boresight is nominally aligned with the transmitter at 0° azimuth, which nominally lies on the positioner rotation axis. Actual misalignments in these quantities were solved for in the analysis, and turned out to be small (~0.1°).

Scans of 360° in azimuth were made at each increment of 5° in rotation from 0° to 355°. In this procedure each point in the pattern is measured twice, the second with the antenna upside-down and at negative positioner azimuth with respect to the first. This otherwise redundant approach allowed scattering effects induced by the asymmetric range to be identified and eliminated.

Fig. 1 gives a three-dimensional representation of the patterns measured for the flight antenna and feed for the 37 H channel. The patterns are obtained as the root sum of squares of the co- and cross-polarized patterns and thus represent the antenna's response to unpolarized radiation (the TMR always views the nadir so that the details of the polarized pattern are unimportant). Fig. 2 shows the coordinate conventions used for the plots and their relationship to the standard spacecraft body-fixed coordinate system.

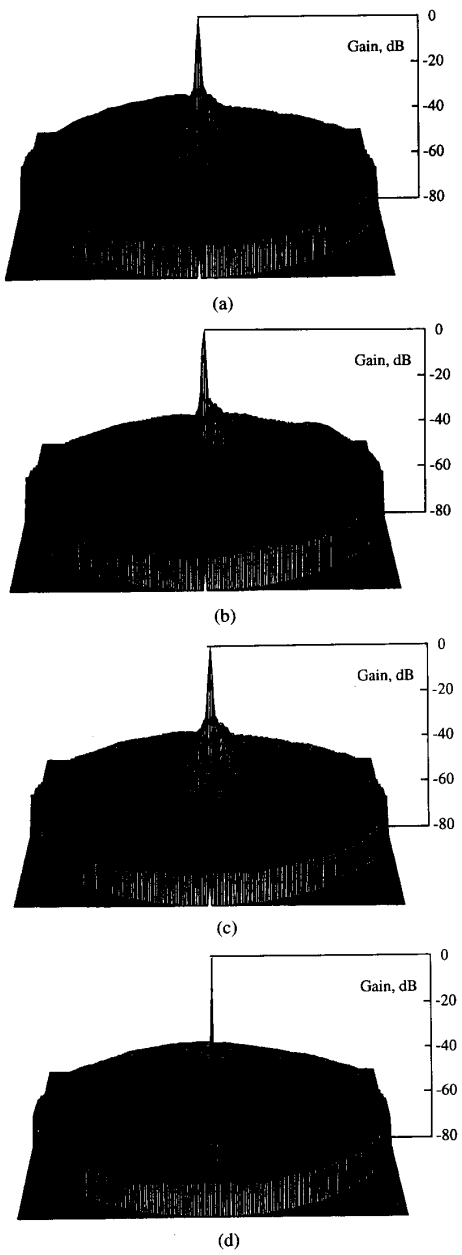

Fig. 1. Three-dimensional representations of the measured 37 H channel pattern for the flight antenna and feed (see explanations in the text). The coordinate system used for the plots are shown in Fig. 2(a). The baseline plane of each plot lies at a level 80 dB below the central peak, and the vertical scale indicates the power gain relative to the central peak. The main lobe at the center of the front hemisphere plots is unresolved on the scale of these plots but is relatively clean and free of detailed structure. The ribbed structure seen in the wing of the main lobe is believed due to the antenna support legs. No significant features are apparent in the far sidelobes.

Fig. 1(a) shows the "normal" pattern in the forward hemisphere obtained for positioner rotations in the range 0° to 175°, where the cut extending from the point at the bottom from edge to the top back edge represents a positioner azimuth scan from South to North on the range at 0° rotation angle, and increasing positioner rotation is presented counter-clockwise on the plot.

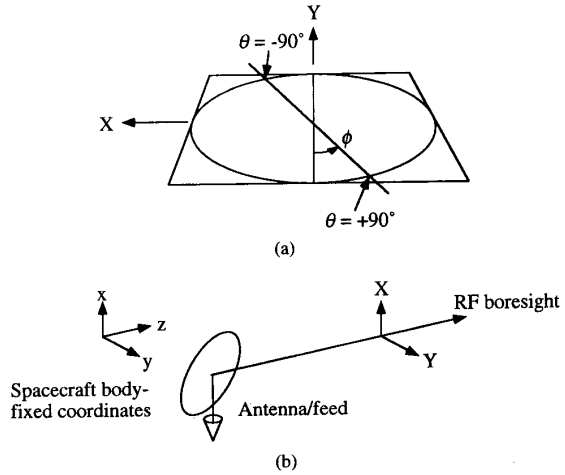

Fig. 2. (a) Coordinate conventions used for the plots in Fig. 1, and (b) their relationship to the spacecraft body-fixed coordinate system.

A ~5° smoothing in rotation and 2° in azimuth has been used to bring out the low-level signals in the plots. The "inverted" plot in Fig. 1(b) shows the pattern obtained from positioner rotations in the range 180° to 355° and displayed in the same antenna reference frame.

If the range were symmetric, both patterns would be identical. Detailed comparisons show that the effect of range scattering is evident on all positioner azimuths in the range ~70° to 110°. Consequently we excised all data within the range 0° to 130° and combined the remaining data to create a "merged" pattern which is free of evident range scattering artifacts, with both hemispheres shown in Fig. 1(c) and (d). The spike in the center of the back-hemisphere merged pattern is a computer-generated artifact to locate the 0 dB level of the plot.

Comparison of the normal and inverted patterns shows that the observed structure repeats even at levels below 50 dB, giving confidence in their reality. The dominant feature is the four-ribbed radial pattern that appears in the wings of the main lobe and extends down to the pattern floor in the neighborhood of 70 dB below the main peak. We believe this pattern to be due to the antenna support legs, which still infringe weakly on the signal path after the feed redesign discussed previously. The pattern is not as apparent as in the original SMMR antenna patterns [6], and demonstrates the success of the feed redesign [1, Table III].

B. Analysis

The measured patterns were analyzed to account for possible systematic errors: non-linearity of the receiver system, an apparent noise floor due to receiver noise at the lowest signal levels, and scattering from the positioner and support structure not representative of the antenna in its final flight configuration. The antenna beam fractions were then obtained by direct integration of the corrected beam patterns.

1. Linearity: The receiver linearity was monitored on each day of the range measurements using a calibrated attenuator to

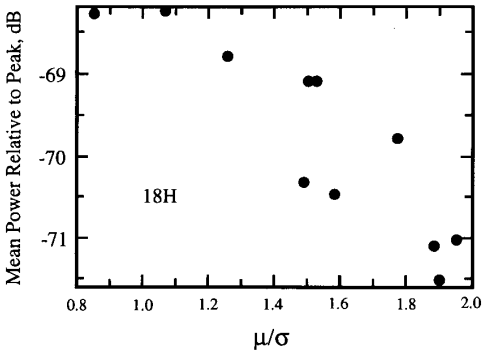

Fig. 3. Ratio μ/σ evaluated from samples of the 18 GHz pattern measurements and plotted against mean power in each sample.

TABLE I
BACKLOBE ARTIFACT BEAM FRACTION

18H	0.0018
21H	0.0011
21V	0.0017
37H	0.0009

TABLE II
FLIGHT ANTENNA BEAM FRACTIONS

Channel	b	c
18H	0.0278 ± 0.0042	0.0049 ± 0.0013
21H	0.0247 ± 0.0041	0.0029 ± 0.0011
21V	0.0316 ± 0.0043	0.0030 ± 0.0012
37H	0.0215 ± 0.0043	0.0037 ± 0.0014

reduce the peak signal through a range of 50 dB. The average of all such linearity measurements was within 0.5 dB or better of nominal values throughout this range, although daily results indicated deviations of about 1 dB below the 30 dB level which were not repeatable and are suspected to be due to drifts in the receiver gains on daily or shorter time scales. We conservatively allow that there are systematic uncertainties of 1 dB in the measured patterns at levels less than 30 dB below the central peak.

2. Noise Floor Corrections: In the range test receiver, the received signal is modulated and detected synchronously by an ac voltmeter. The output voltage of the receiver is ideally proportional to the input signal voltage, and the antenna power gain is obtained as the square of this quantity. Hence the noise on this voltage leads to a power which is always positive and produces a false "noise floor" on the measured pattern when the signal is comparable to or less than this floor. This can result in a systematic bias in the integrated beam fractions. Specifically, random noise at the input to the voltmeter leads to an average measured output power

$$\langle p \rangle \propto \langle v^2 \rangle = \langle s^2 \rangle + 2\sigma^2 \tag{7}$$

where σ is the rms voltage of the noise both in and out of phase with the modulated signal s. Hence we may model the noise as an additive constant power everywhere in the measured pattern.

This noise floor was determined by examining the statistics of the noise in regions of the measured pattern suspected to have no detectable sidelobes and verifying that the distribution of measured voltages in these regions followed the modeled noise. The noise was modeled as a voltage with a Rayleigh-distributed amplitude and randomly distributed phase [9]. The probability distribution function for this noise model has a mean (μ) and a standard deviation (σ) with the property that the ratio μ/σ is a constant given by

$$\mu/\sigma = (4/\pi - 1)^{-1/2} \approx 1.91. \tag{8}$$

In the presence of a signal, however, this ratio shifts quickly away from this constant. Fig. 3 shows the ratio μ/σ computed from samples from the 18 GHz pattern measurements taken from 30° azimuthal slices within a polar angle of 75° to 135°, and plotted against the mean power level in each sample. The lowest power levels correspond to the data that is most nearly Rayleigh distributed, and appear to be samples of the receiver noise floor only. More detailed analysis indicates that the noise floor in all channels is 71±2 dB below the central peak.

3. Backlobe Artifacts: All pattern measurements show a significant backlobe beyond a polar angle of about 155°. At this position the antenna faces the positioner structure which, although wrapped in absorbing material, is nevertheless able to scatter a small amount of signal back into the receiver. There is no reason to expect a significant backlobe in this region under flight conditions, and we have considered the gain beyond 155° to be zero and have corrected our beam fraction calculations accordingly. The beam fraction found in this artifact (i.e., the quantity given by (5) for θ_2 =155°) is given in Table I.

4. Beam Fractions: A computer program was written to perform a computation of the beam fractions according to (4) and (5) by numerical quadrature. As a check, we also used the program originally developed by R. Cofield to compute beam solid angles for the SMMR antenna patterns, which were measured with the same equipment and digitized in the same format [6]. Our results are given in Table II. They include the subtraction of the noise floor and assume no power is present in the beam beyond a polar angle of 155°. The results from the two independent computations differ by no more than 0.0005 in all cases.

The uncertainties in Table II are derived from a quadrature addition of the uncertainty in the noise floor removal with that due to a 1 dB uncertainty in the power pattern at all levels less than 30 dB below the central peak. The linearity uncertainty dominates the uncertainty in the beam fraction b, while both sources contribute about equally to the net uncertainty in the beam fraction c.

IV. ERROR ANALYSIS FOR THE APC ALGORITHM

We consider that we begin with calibrated antenna temperatures with the objective of obtaining the average brightness temperature in the respective TMR footprints. The error analysis here then concentrates on the uncertainties incurred in

TABLE III
APC ERRORS

Channel:	18H	21H	21V	37H
Error terms:				
E(b)	0.06 K	0.05 K	0.06 K	0.06 K
E(c)	0.27 K	0.22 K	0.25 K	0.28 K
$E(T_a)$	0.59 K	0.59 K	0.56 K	0.55 K
$E(T_e)$	0.55 K	0.48 K	0.62 K	0.62 K
$E(T_c)$	<0.001 K	<0.001 K	<0.001 K	<0.001 K
Net APC Uncertainty:	0.85 K	0.79 K	0.87 K	0.88 K

the APC algorithm expressed by (6). Additional uncertainties result from the approximation that the main beam brightness temperatures $T_{\rm mb}$ obtained by this algorithm represents the actual brightness temperatures in the much smaller altimeter footprints, and are discussed in Section V.

Each of the five quantities contained in (6) possess independent errors, so that we may express the total uncertainty in the brightness temperature estimate $T_{\rm mb}$ as

$$\Delta T_{\rm mb} = \left[\sum_{i=1}^{5} E^2(q_i)\right]^{1/2} \tag{9}$$

where the error terms

$$E(q_i) = \left|\frac{\partial T_{\rm mb}}{\partial q_i}\right| \Delta q_i \tag{10}$$

and q_i indexes the quantities b, c, T_a, T_e, and T_c. The 1-sigma uncertainties of these quantities are expressed as Δq_i. Using (6) to evaluate the $E(q_i)$, we obtain

$$E(b) = \frac{1}{(1-b-c)^2}[T_a - T_e + c(T_e - T_c)]\Delta b \tag{11}$$

$$E(c) = \frac{1}{(1-b-c)^2}[T_a - T_c - b(T_e - T_c)]\Delta c \tag{12}$$

$$E(T_a) = \frac{1}{1-b-c}\Delta T_a \tag{13}$$

$$E(T_e) = \frac{b}{1-b-c}\Delta T_e \tag{14}$$

$$E(T_c) = \frac{c}{1-b-c}\Delta T_c. \tag{15}$$

We evaluated these expressions using nominal globally-averaged values for T_a and T_e from a radiative transfer model and the results of the previous section for the beam fractions and their uncertainties. The results are given in Table III. T_c is effectively the 2.7°K blackbody temperature of the cosmic background, with negligible contributions from the sun, moon, and other sources. T_c must be corrected at each frequency to account for departures from the Rayleigh-Jeans law [7]. The calibration uncertainties ΔT_a are taken from [1].

The radiative transfer model [2] used a data base consisting of more than 4000 radiosondes launched from five island sites whose latitudes ranged from 8° to 52° (see Table IV), for which the viewing-angle dependent brightness temperatures were computed for the 21 and 37 GHz TMR frequencies.

TABLE IV
ISLAND SITES USED TO DETERMINE T_e AND ΔT_e

Site	Latitude	# Raobs	21 GHz T_e	21 GHz ΔT_e	37 GHz T_e	37 GHz ΔT_e
Kwajalein	8 44N	574	208	17	195	30
Pago	14 20S	1073	202	16	192	29
Kingston	17 56N	1030	196	16	184	24
Midway	28 13N	838	175	18	167	21
Adak	51 53N	919	162	28	178	38

TABLE V
T_e VERSUS LATITUDE

Latitude:	21 GHz	37 GHz	Latitude:	21 GHz	37 GHz
±0	209 K	196 K	±40	167 K	169 K
±5	208	195	±45	165	171
±10	205	194	±50	163	176
±15	201	192	±55	161	180
±20	194	182	±60	159	183
±25	181	172	±65	158	185
±30	173	170	±70	157	186
±35	170	169	±75-90	156	186

T_e was computed from these using the beam patterns of the previous section, while T_a was determined from the computed nadir brightness temperatures using (3) and the beam fractions of Table II. Table V gives a smoothed latitudinally-dependent fit to the seasonally-averaged values of T_e shown in Table IV. ΔT_e was obtained by first finding the RMS distribution of values for individual days around this model at each site as shown in Table IV, and then averaging these for all sites to obtain 19°K and 28°K respectively for the 21 and 37 GHz channels. The values for $E(T_e)$ given in Table III thus represent approximate global means. The values given for 18 GHz were estimated based on the 21 GHz results. This method overestimates the error in that the contribution to the TMR signal through the sidelobes averages an area approximately 2000 km in diameter, while the present estimate is based on variabilities at single points.

The results indicate that the net APC algorithm error, including the radiometer calibration error, is in the range 0.79–0.88°K. The uncertainty due to the variable emission seen in the 2–3% beam fraction that falls outside the main beam but onto the Earth is comparable to the radiometer calibration error, and is a significant contributor to our current estimate of the net APC algorithm error. The $E(T_e)$ error could undoubtedly be reduced by using a more sophisticated approach toward the estimation of T_e than taking seasonal averages versus latitude. A better estimate of this error can be obtained directly from the TMR flight data as it becomes available. The impact of this error on the net path delay correction is not as large as might appear, however, because the errors are correlated among the TMR channels so that they tend to cancel in the path delay retrieval algorithm—this point is discussed further in [2].

V. Errors Due to Beam Size Differences

The assumption that the main beam brightness temperature yields an accurate estimate of the brightness temperature of the altimeter footprint depends on the variability of contributing atmospheric parameters on spatial scales from the size of the altimeter footprint (few km) to that of the three TMR main beams (few tens of km). We estimate the uncertainties incurred by this assumption in this section. We will first assume that the TMR beams are all equal, which allows us to use a statistical model for spatial, path delay variations to compute the decorrelation between path delay averaged over the greatly differing footprints of the altimeter and the TMR. This error is most conveniently expressed directly in terms of path delay. We then address the additional uncertainty caused by the beam size differences at the three TMR frequencies.

A. Altimeter/TMR Footprint Differences

Because the path delay retrieval algorithm is nearly linear in the brightness temperature variables, it follows that the path delay derived from brightness temperatures which are uniformly averaged over a given area will closely approximate the path delay obtained directly with the same averaging. We assume that the TMR footprints are all described by the same antenna gain pattern $G_{\mathrm{TMR}}(\mathbf{x}-\mathbf{x}_{\mathrm{TMR}})$ where $\mathbf{x}$ is a horizontal position vector and $\mathbf{x}_{\mathrm{TMR}}$ is the TMR beam center, while the altimeter footprint is equivalently described by $G_{\mathrm{alt}}(\mathbf{x}-\mathbf{x}_{\mathrm{alt}})$. The average path delay over either footprint is given by

$$P_i = \int P(\mathbf{x}) G_i(\mathbf{x}-\mathbf{x}_i) d\mathbf{x} \tag{16}$$

where $P(\mathbf{x})$ is the vertical path delay at a point $\mathbf{x}$ on the ground and the subscript i denotes either the TMR or the altimeter. G_i is normalized so that

$$\int G_i(\mathbf{x}-\mathbf{x}_i)\, d\mathbf{x} = 1. \tag{17}$$

The RMS difference between the altimeter and TMR path delays can be written as

$$\sigma_A = \langle [P_{\mathrm{TMR}} - P_{\mathrm{alt}}]^2 \rangle^{1/2} \tag{18}$$

where the expectation represents an ensemble average and σ_A is an implicit function of the altimeter and TMR footprints and their relative centers. Ideally the altimeter and TMR are aligned, but it is easy to generalize for the case of a misalignment. In the Appendix we show that σ_A may be computed with knowledge of the respective averaging functions and a statistical model for atmospheric path delay correlation. For the specific case of the TMR and altimeter beams, we may write (A9) as

$$\sigma_A = \left\{ -\frac{1}{2} \int\int \sigma_p^2(\mathbf{x}-\mathbf{x}') [G_{\mathrm{TMR}}(\mathbf{x}-\mathbf{x}_{\mathrm{TMR}}) - G_{\mathrm{alt}}(\mathbf{x}-\mathbf{x}_{\mathrm{alt}})] \times [G_{\mathrm{TMR}}(\mathbf{x}-\mathbf{x'}_{\mathrm{TMR}}) - G_{\mathrm{alt}}(\mathbf{x}'-\mathbf{x}_{\mathrm{alt}})] d\mathbf{x} d\mathbf{x}' \right\}^{1/2}. \tag{19}$$

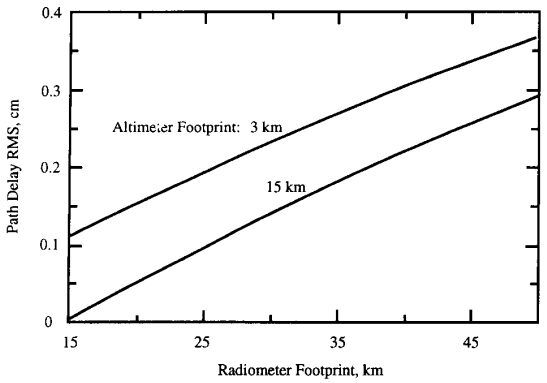

Fig. 4. Typical RMS path delay variations between path delay averaged over nominal altimeter footprints, relative to path delay averaged at the same time over the nominal radiometer footprint indicated on the horizontal scale.

The quantity

$$\sigma_p^2(\mathbf{x}-\mathbf{x}') = \langle [P(\mathbf{x}) - P(\mathbf{x}')]^2 \rangle \tag{20}$$

incorporates the statistical model for spatial path delay variations. The functional form

$$\sigma_p^2(\mathbf{x}-\mathbf{x}') = a|\mathbf{x}-\mathbf{x}'|^p \tag{21}$$

where a and b are empirically-determined constants, has been found to describe the behavior of path delay variations for a wide variety of atmospheric conditions [10], [11].

Fig. 4 shows the RMS path delay computed for a range of TMR and altimeter-sized footprints using typical values for a and p obtained from [10]. Taking 3 km as the altimeter footprint and 40 km as representative of the TMR footprint, we find $\sigma_A \approx 0.3$ cm.

B. TMR Frequency-Dependent Footprint Differences

Unequal beam sizes at the three TMR frequencies leads to further errors because the respective brightness temperatures do not represent averages over equal areas. The frequency-dependent spatial structure in brightness temperature due to water vapor, cloud liquid water, and sea surface brightness variations then produces beam-averaged brightness temperature differences that are uncorrelated with path delay. For example, water vapor variations will result in such brightness temperature differences, the magnitude of which may be readily estimated by the statistical approach described in the previous section. Taking the same model used to derive the results shown in Fig. 4, we have computed the RMS path delay differences expected among the TMR beams and used these to estimate the corresponding brightness temperature differences based on the mean linear retrieved approximation given by [2, (20)]. We find that random brightness temperature errors from this source are about 0.1°K or less, and are thus of minor significance.

Variations in sea surface brightness and cloud liquid can produce significant brightness temperature differences. We are unaware of statistical models for the spatial structure of these variations comparable to that for water vapor; consequently, we have not carried out a comparable analysis.

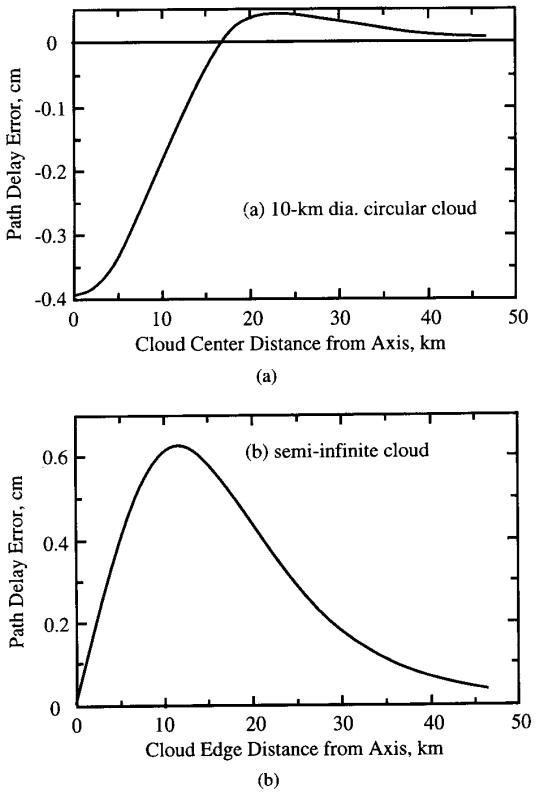

Fig. 5. Path delay errors caused in a typical atmosphere by (a) a 10 km circular cloud, and (b) a semi-infinite cloud edge, each with 2000 μ precipitable water liquid, moving though the TMR beams.

Instead, we resort to a reasonable worst-case analysis to estimate the possible effects of cloud liquid variations, which we expect to cause the largest effect. Liquid water is highly variable on scales much less than the beam footprints, and typical variations can produce sharp brightness temperature contrasts. We consider two examples in Fig. 5: heavy clouds (2000 μ integrated liquid content) with circular (Fig. 5(a)) and semi-infinite edge (Fig. 5(b)) geometries, which approximate structure likely to be encountered along the TMR ground track. We computed the beam-averaged brightness temperature for a typical atmosphere as the beams are swept across the clouds in each example, and then used the approximate linear algorithm to calculate the corresponding effect on path delay shown in the figure. We interpret these results to indicate that the instantaneous perturbation to path delay can be significant and will exceed a centimeter in extreme cases, but that the time-averaged error is likely to be a relatively minor element in the overall error budget. The effect averaged over all views of a given cloud configuration will be zero, so that no net bias is introduced.

One can approximately equalize the beams along the ground-track dimension by taking selectively weighted averages of the measurements, suggesting the possibility of reducing errors caused by unequal beamwidths by extending the brightness temperature algorithm to include such averaging. To investigate this, we considered a model in which the field of view

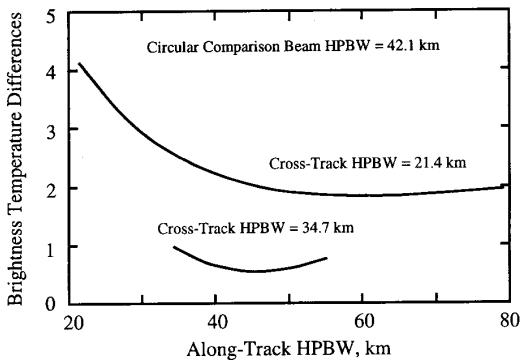

Fig. 6. Differences between the relative brightness temperatures obtained from a large circular beam and each of two smaller beams as the latter are stretched in one dimension. The scene viewed is assumed to consist of a random distribution of point sources. The vertical scale is arbitrary. The effective footprints of the measurements can be stretched along-track by using selectively weighted averages of the data. The examples demonstrate that measurement errors due to the unequal beam sizes of the TMR can be reduced by about a factor of two.

contains randomly scattered point sources generally descriptive of cloud structure. We computed brightness temperatures from this model for beam patterns of varying shapes and sizes. Fig. 6 shows the behavior of the differences between the relative brightness temperatures obtained from a large beam and each of two smaller beams as the latter become stretched in one dimension. Such "stretching" can effectively be obtained by a symmetric Gaussian weighting over measurements preceding and following a given measurement. The relative beam geometries indicated in Fig. 6 were chosen to be descriptive of the TMR beams. The results indicate that a reduction by about a factor of two can be achieved in the brightness temperature differences between two beams if the along-track dimension of the smaller beam is stretched to slightly exceed that of larger beam.

Appendix
Spatially-Averaged Wet Path Delay Correlation Structure

Let us assume that we know the RMS difference in the integrated path delay between two discrete paths through the atmosphere as a function of the horizontal separation between the paths. We wish to extend this point-correlation structure to the case where each path delay is itself a spatially averaged delay.

Let a spatially-averaged path delay be expressed as

$$P_i = \int P(\mathbf{x}) G_i(\mathbf{x} - \mathbf{x}_i) d\mathbf{x} \tag{A1}$$

where $\mathbf{x}$ is a horizontal position vector, $P(\mathbf{x})$ is the vertical path delay at the point $\mathbf{x}$, and $G_i(\mathbf{x} - \mathbf{x}_i)$ is an averaging function (e.g., an antenna pattern) centered at $\mathbf{x_i}$ and normalized so that

$$\int G_i(\mathbf{x} - \mathbf{x}_i) d\mathbf{x} = 1. \tag{A2}$$

For simplicity we assume that all quantities are defined on an infinite plane and that the integrations are taken over the entire

plane. In particular, we consider that the statistical properties of $P(\mathbf{x})$ are uniform with $\mathbf{x}$. The RMS difference between two such spatially-averaged path delays, σ_A, can be written as

$$\sigma_A = \langle [P_1 - P_2]^2 \rangle^{1/2} \tag{A3}$$

where the brackets indicate an ensemble average (e.g., over the plane), and σ_A is implicitly a function of the averaging functions G_1 and G_2 and their separation $\mathbf{x_1} - \mathbf{x_2}$. Expanding using (A1), we have

$$\begin{aligned}\sigma_A &= \left\langle \left[\int P(\mathbf{x}) \{G_1(\mathbf{x} - \mathbf{x_1}) - G_2(\mathbf{x} - \mathbf{x_2})\} d\mathbf{x} \right]^2 \right\rangle^{1/2} \\ &= \left\langle \int \int P(\mathbf{x}) P(\mathbf{x}') \{G_1(\mathbf{x} - \mathbf{x_1}) - G_2(\mathbf{x} - \mathbf{x_2})\} \right. \\ &\qquad \left. \times \{G_1(\mathbf{x}' - \mathbf{x}) - G_2(\mathbf{x}' - \mathbf{x_2})\} d\mathbf{x} d\mathbf{x}' \right\rangle^{1/2} \\ &= \left[\int \int \langle P(\mathbf{x}) P(\mathbf{x}') \rangle \{G_1(\mathbf{x} - \mathbf{x_1}) - G_2(\mathbf{x} - \mathbf{x_2})\} \right. \\ &\qquad \left. \times \{G_1(\mathbf{x}' - \mathbf{x_1}) - G_2(\mathbf{x}' - \mathbf{x_2})\} d\mathbf{x} d\mathbf{x}' \right]^{1/2}.\end{aligned} \tag{A4}$$

We rewrite

$$\langle P(\mathbf{x}) P(\mathbf{x}') \rangle \equiv \frac{1}{2} [\langle P^2(\mathbf{x}) \rangle + \langle P^2(\mathbf{x}') \rangle - \langle [P(\mathbf{x}) - P(\mathbf{x}')]^2 \rangle]. \tag{A5}$$

Now

$$\langle P^2(\mathbf{x}) \rangle = \langle P^2(\mathbf{x}') \rangle \equiv \langle P^2 \rangle \tag{A6}$$

and we assume the statistical behavior

$$\langle [P(\mathbf{x}) - P(\mathbf{x}')]^2 \rangle \equiv \sigma_p^2(\mathbf{x} - \mathbf{x}') \tag{A7}$$

whereupon substitution into (A4) yields

$$\begin{aligned}\sigma_A = \left[\langle P^2 \rangle \left[\int [G_1(\mathbf{x} - \mathbf{x_1}) - G_2(\mathbf{x} - \mathbf{x_2})] d\mathbf{x} \right]^2 \right. \\ - \frac{1}{2} \int \int \sigma_p^2(\mathbf{x} - \mathbf{x}') [G_1(\mathbf{x} - \mathbf{x_1}) - G_2(\mathbf{x} - \mathbf{x_2})] \\ \left. \times [G_1(\mathbf{x}' - \mathbf{x_1}) - G_2(\mathbf{x}' - \mathbf{x_2})] d\mathbf{x} d\mathbf{x}' \right]^{1/2}.\end{aligned} \tag{A8}$$

The first term in (A8) vanishes because of the normalization of (A2), which leaves the desired result

$$\begin{aligned}\sigma_A = \left\{ -\frac{1}{2} \int \int \sigma_p^2(\mathbf{x} - \mathbf{x}') [G_1(\mathbf{x} - \mathbf{x_1}) - G_2(\mathbf{x} - \mathbf{x_2})] \right. \\ \left. \times [G_1(\mathbf{x}' - \mathbf{x_1}) - G_2(\mathbf{x}' - \mathbf{x_2})] d\mathbf{x} d\mathbf{x}' \right\}^{1/2}.\end{aligned} \tag{A9}$$

The quantity σ_A may be evaluated using (A9) with knowledge of the patterns G_1 and G_2, and a model for the two-point RMS difference σ_p^2.

Equation (A9) can be tested for two special cases. First, let the two antenna patterns be identical, $G_1 = G_2$ and concentric so that $\mathbf{x_1} = \mathbf{x_2}$. Then the integrand of (A9) vanishes and we obtain $\sigma_A = 0$ as expected. In the second case, let the two antenna patterns approach delta functions centered on different points, i.e., $\mathbf{x_1} \neq \mathbf{x_2}$. Equation (A9) becomes

$$\begin{aligned}\sigma_A &= \left\{ -\frac{1}{2} \int \int \sigma_p^2(\mathbf{x} - \mathbf{x}') [\delta(\mathbf{x} - \mathbf{x_1}) - \delta(\mathbf{x} - \mathbf{x_2})] \right. \\ &\qquad \left. \times [\delta(\mathbf{x}' - \mathbf{x_1}) - \delta(\mathbf{x}' - \mathbf{x_2})] d\mathbf{x} d\mathbf{x}' \right\}^{1/2} \\ &= \left\{ -\frac{1}{2} \int [\sigma_p^2(\mathbf{x_1} - \mathbf{x}') - \sigma_p^2(\mathbf{x_2} - \mathbf{x}')] \right. \\ &\qquad \left. \times [\delta(\mathbf{x}' - \mathbf{x_1}) - \delta(\mathbf{x}' - \mathbf{x_2})] d\mathbf{x}' \right\}^{1/2} \\ &= \left\{ -\frac{1}{2} [\sigma_p^2(\mathbf{x_1} - \mathbf{x_1}) - \sigma_p^2(\mathbf{x_2} - \mathbf{x_1}) \right. \\ &\quad \left. - \sigma_p^2(\mathbf{x_1} - \mathbf{x_2}) + \sigma_p^2(\mathbf{x_2} - \mathbf{x_2})] \right\}^{1/2} \\ &= \sigma_p(\mathbf{x_1} - \mathbf{x_2})\end{aligned} \tag{A10}$$

or the point correlation RMS, as expected.

ACKNOWLEDGMENT

The authors would like to express particular appreciation to Paul Batelaan of JPL for his assistance with the antenna pattern measurements, to Richard Cofield of JPL for providing data and algorithms used in the SMMR antenna pattern analysis, and to Dudley Chelton of Oregon State University and other members of the TOPEX Science Team for careful review and helpful criticism during the performance of this work.

REFERENCES

[1] C. S. Ruf, S. J. Keihm, and M. A. Janssen, "TOPEX/Poseidon Microwave Radiometer (TMR): I. Instrument description and antenna temperature calibration," *IEEE Trans. Geosci. Remote Sensing*, vol. 33, pp. 125–137, Jan. 1995.

[2] S. J. Keihm, M. A. Janssen, and C. S. Ruf, "TOPEX/Poseidon Microwave Radiometer (TMR): III. Wet troposphere range correction algorithm and pre-launch error budget," *IEEE Trans. Geosci. Remote Sensing*, vol. 33, pp. 147–161, Jan. 1995.

[3] E. G. Njoku, J. M. Stacey, and F. T. Barath, "The Seasat Scanning Multichannel Radiometer (SMMR): Instrument description and performance," *IEEE J. Ocean. Eng.*, vol. OE-5, pp. 100–115, 1980.

[4] E. A. Francis, "Calibration of the NIMBUS-7 SMMR," M.S. thesis, Dept. of Oceanography, Oregon State University, Corvalis, OR, 1987.

[5] A. S. Milman and T. T. Wilheit, "Sea surface temperature from the scanning multichannel radiometer on NIMBUS-7," *J. Geophys. Res.* vol. 90, no. C6, pp. 11631–11641, 1985.

[6] E. G. Njoku, E. J. Christensen, and R. T. Cofield, "The Seasat scanning multichannel radiometer (SMMR): Antenna pattern corrections—development and implementation," *IEEE J. Ocean. Eng.*, vol. OE-5, pp. 125–137, 1980.

[7] M. A. Janssen, "Introduction to the microwave remote sensing of atmospheres," in *Atmospheric Remote Sensing by Microwave Radiometry*, M. A. Janssen, Ed. New York: Wiley, 1993, ch. 1.

[8] "TOPEX radar altimeters systems specification," Wallops Doc. WFF-672-85-004004, Rev. 6, 1989.

[9] A. Popoulis, *Probability, Random Variables, and Stochastic Processes*. New York: McGraw-Hill, 1984.

[10] J. W. Armstrong and R. A. Sramek, "Observations of tropospheric phase scintillations at 5 GHz on vertical paths," *Radio Sci.* vol. 17, pp. 1579–1586, 1982.

[11] A. R. Thompson, J. M. Moran, and G. W. Swenson, Jr., *Interferometry and Synthesis in Radio Astronomy*. New York: Wiley, 1986, pp. 406–439.

Michael A. Janssen, for a photograph and biography, see pg. 137 of this issue of this TRANSACTIONS.

Christopher S. Ruf (S'85–M'87–SM'92), for a photograph and biography, see pg. 136 of this issue of this TRANSACTIONS.

Stephen J. Keihm, for a photograph and biography, see pg. 137 of this issue of this TRANSACTIONS.